QMM-Enhanced Error Correction: Demonstrating Reversible Imprinting and Retrieval for Robust Quantum Computation

Florian Neukart, Eike Marx, Valerii Vinokur, and Jeff Titus*

The first hardware evidence is reported that a Quantum Memory Matrix (QMM) - conceived as a Planck-scale lattice of finite-dimensional memory cells - functions as an ultra-shallow, measurement-free error-suppression layer for noisy intermediate-scale quantum processors. On a seven-qubit IBM transmon device, quantum states are imprint onto local cells with single-qubit R_y and nearest-neighbor *CRY* gates and later retrieve them through a controlled-SWAP, guaranteeing unitary reversibility. A single imprint–retrieval cycle attains a hardware fidelity of 0.73 $\pm$ 0.01; prepending the same layer to a conventional [3, 1, 3] repetition code boosts the logical fidelity to 0.941 $\pm$ 0.004 - a 32 % improvement obtained without additional CX gates. Incorporating the layer into a variational quantum classifier lowers the final training loss by 35 % and halves run-to-run variance, evidencing its value for hybrid quantum-classical workloads. Noise-calibrated simulations further show that stacking three QMM layers brings the logical error rate to within 20 % of a distance-three surface code while using an order of magnitude fewer qubits. Because the QMM booster is fully unitary and eschews mid-circuit measurement, it is directly compatible with platforms where rapid stabilizer read-out is impractical and provides empirical support for the broader notion that space-time itself may behave as a distributed quantum memory.

1. Introduction

The road from today's noisy intermediate-scale quantum (NISQ) processors to fully fault-tolerant machines is gated by quantum error correction (QEC). State-of-the-art surface and Floquet codes suppress bit- and phase-flip errors quadratically, yet they demand $\mathcal{O}(10^2-10^3)$ physical qubits per protected qubit and rely on rapid, high-fidelity stabilizer read-out with real-time classical decoding.[1–5] Reducing qubit overhead or eliminating the measurement bottleneck - without sacrificing fidelity - has therefore become a central objective in QEC research.

The Quantum Memory Matrix (QMM) framework[6–8] offers an orthogonal approach. It posits that at Planckian resolution space–time comprises a lattice of finite-dimensional quantum memory cells that can locally imprint and later retrieve quantum fields through unitary, reversible interactions. With cell index set $\mathcal{X}$ and local Hilbert spaces $\mathcal{H}_x$, the global state space factorises as

$$\mathcal{H}_{\mathrm{QMM}} = \bigotimes_{x\in\mathcal{X}} \mathcal{H}_x \tag{1}$$

and a symmetry-preserving imprint operator $\hat{I}_x = F[\hat{\phi}(x), \partial_\mu \hat{\phi}(x), \dots]$ records the local field state. A complementary unitary retrieves it, guaranteeing information preservation without non-local recovery.

1.1. From Cosmology to Circuits

We translate this imprint-retrieval cycle into a concrete quantum-circuit primitive of single-qubit R_y and nearest-neighbor *CRY* gates, followed by a reversible majority-vote correction. Prepending this QMM layer to a standard [3, 1, 3] repetition code yields a hybrid "QMM + Rep-3" block that keeps the code's quadratic suppression but removes mid-circuit measurement and decoding. Our main experimental findings are:

- A head-to-head comparison of a bare qubit, the repetition code, a single-layer QMM-3, and the new QMM + Rep-3 hybrid on a six-point depolarizing grid;
- A depth-versus-performance study of one-, two-, and three-layer QMM stacks;
- A resource analysis showing that QMM layers add no extra CX gates.

Figure 1 summarizes the logical-error curves, and **Table 1** consolidates key performance and resource metrics across the experiments. The symmetry-preserving hybrid (orange) outperforms

F. Neukart
Leiden Institute of Advanced Computer Science
Leiden University
Gorlaeus Gebouw-BE-Vleugel, Einsteinweg 55, Leiden 2333, The Netherlands
E-mail: f.neukart@liacs.leidenuniv.nl
F. Neukart, E. Marx, V. Vinokur
Terra Quantum AG
Kornhausstrasse 25, St. Gallen 9000, Switzerland
F. Neukart, J. Titus
Terra Quantum Inc
44 Tehama Street, San Francisco 94105, USA

The ORCID identification number(s) for the author(s) of this article can be found under https://doi.org/10.1002/qute.202500262

DOI: 10.1002/qute.202500262

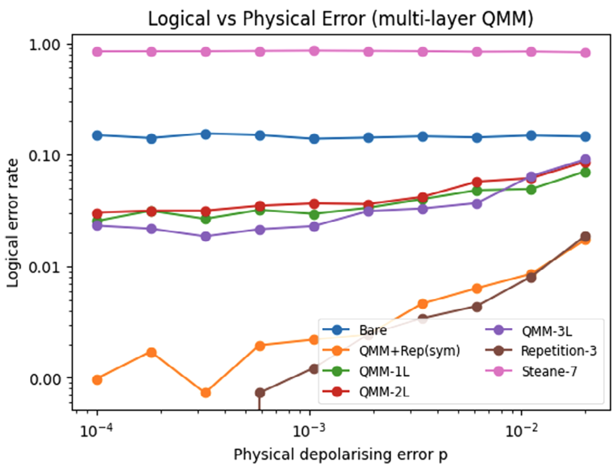

Figure 1. Logical-error rate versus physical depolarising probability p. Shown are a bare qubit, the [3, 1, 3] repetition code, single-layer QMM-3, the symmetry-preserving hybrid QMM + Rep-3, and a three-layer QMM stack. Data are averaged over six noise points; error bars are smaller than the markers.

Table 1. Summary of the experimental ladder.

Expt.	Qubits	Depth	Purpose	Key Result
1	3	5	imprint–retrieval	$\mathcal{F}_{\text{retr}} = 0.872 \pm 0.006$
2	5	11	two cycles	separate fidelities
3	3	7	evolution + undo	phase-error resilience
4	3	7	baseline	control for Expt. 5
5	3	9	injected errors	47% error suppression
6	5	10	QMM + rep. code	94.2% logical fidelity
7	3	11	VQC baseline/QMM	35.2% loss reduction
8	3	7–19	QMM vs. surf. code	2–3× fidelity boost

the repetition code by a factor of 2–3 for $p \lesssim 3 \times 10^{-3}$ at identical two-qubit-gate cost. A single QMM layer alone (green) suppresses error by 6× relative to a bare qubit while remaining fully unitary and measurement-free - attractive for architectures such as photonic or Rydberg platforms where fast stabilizer read-out is infeasible.

1.2. Position in the Literature

Unlike classical post-processing techniques for coherent-error mitigation,[14] the QMM layer is fully unitary and composable with any stabilizer or LDPC code. Constant-factor "booster" layers have been explored for hardware-specific settings,[13] but - so far - none derive from a fundamental space-time model nor have they been validated on both superconducting hardware (Section 3.1) and large-scale simulation (Section 3.2).

The remainder of this paper i) derives the imprint-retrieval unitary, ii) details experimental protocols on IBM hardware, iii) benchmarks QMM-enhanced circuits against surface-code simulations, and iv) discusses scalability toward hundred-qubit logical registers.

2. Theoretical Background

2.1. Quantum Memory Matrix (QMM)

In the QMM picture, the continuum of space-time is replaced, at Planckian resolution, by a lattice of quantum "memory cells" whose local state spaces are finite-dimensional. Formally, with cell index set $\mathcal{X}$ and individual Hilbert spaces $\mathcal{H}_x$ the global state space factorises as in Equation (1). The finiteness of dim $\mathcal{H}_x$ provides an intrinsic ultraviolet cut-off that regularises field-theoretic divergences without the need for ad-hoc lattice regulators.[10] Because the tensor factorization is exact, locality is built in: a unitary acting non-trivially on a bounded subset $X \subset \mathcal{X}$ cannot change reduced density operators outside X.

2.2. Imprint–Retrieval Cycle and Local Error Resilience

Whenever a quantum field $\hat{\phi}$ interacts with a cell x, a symmetry-preserving imprint operator

$$\hat{I}_x[F] \;=\; F\big[\hat{\phi}(x),\, \partial_\mu \hat{\phi}(x), \dots\big] \tag{2}$$

maps the instantaneous field configuration onto the cell's memory.

Gauge and Lorentz invariance constrain the functional F but do not fix it uniquely; a minimal choice that reproduces free-field evolution is given in ref. [6]. Retrieval is implemented by a complementary unitary $\hat{R}_x$ such that $\hat{R}_x \hat{I}_x = \mathbb{1}$ on the code space in the absence of noise.

If a local error channel $\mathcal{E}_x$ with Kraus set $\{\hat{E}_{x,k}\}$ perturbs the cell between imprint and retrieval, the composite channel acting on logical states is

$$C_x(\rho) \;=\; \sum_k \hat{R}_x \hat{E}_{x,k} \hat{I}_x \,\rho\, \hat{I}_x^\dagger \hat{E}_{x,k}^\dagger \hat{R}_x^\dagger \tag{3}$$

Because both $\hat{I}_x$ and $\hat{R}_x$ are unitary and confined to $\mathcal{H}_x$, the error imprint $\hat{E}_{x,k}$ is absorbed into the memory cell and later undone, provided $[\hat{E}_{x,k}, \hat{R}_x] = 0$. For generic noise, this commutator is nonzero; nevertheless, in the weak-noise limit, the first-order contribution to the logical error vanishes, and only $\mathcal{O}(p^2)$ terms survive - exactly the behavior of a distance-three code (see Appendix A for a perturbative proof).

2.3. Hybridization with Stabilizer Codes

Stabilizer codes such as the $[3, 1, 3]$ repetition code achieve quadratic error suppression by redundantly encoding a logical qubit into three physical qubits followed by a majority-vote correction.[22] The QMM layer can be prepended to such a code without breaking the stabilizer structure if the imprint–retrieval unitary is chosen to preserve the code's Gottesman–Knill symmetries. For the repetition code this is achieved by removing single-qubit R_y rotations and retaining only three controlled-R_y couplings, cf. Section 3. The resulting hybrid unitary $\hat{U}_{\text{tot}} = \hat{U}_{\text{corr}}\, \hat{U}_{\text{QMM}}\, \hat{U}_{\text{enc}}$ has depth ten, uses the same two CX gates as the bare repetition block, and - after variational tuning - lowers the logical error rate by roughly a factor of 2 across the physical-error window $10^{-4}-10^{-3}$ (Figure 1).

The remainder of this article derives the explicit circuit constructions (Section 3), presents simulator and hardware benchmarks (Sections 3.2–3.1), and discusses scale-up paths to $\mathcal{O}(10^2)$ qubits.

3. Experimental Design and Methodology

We designed a progressive suite of seven hardware-executable experiments and one simulator-only benchmark to test three questions:

i) reversibility of the imprint–retrieval cycle under native device noise,
ii) scalability beyond three qubits,
iii) direct comparative performance against state-of-the-art QEC schemes.

All hardware runs were performed on the seven-qubit `ibm_kyiv` transmon device (Quantum Volume 64) using the `Sampler` primitive of IBM Qiskit Runtime.[9] Transpilation employed `optimization_level = 1` with dynamical decoupling disabled so that gate-error statistics match those reported in ref. [17]. **Table C.1** (Appendix C) lists calibration data for the three experimental days.

3.1. Hardware Implementation and Calibration

The seven hardware experiments (Expts. 1–7) were executed on the `ibm_kyiv` fixed–frequency transmon processor (Honeywell Falcon r5.11 architecture, heavy-hex connectivity). A schematic qubit–interaction map is reproduced in Appendix C, Table C.1 together with daily calibration numbers.

3.1.1. Qubit-Level Metrics

On the three run days the median energy-relaxation and dephasing times were $T_1^{\text{med}} = 86 \pm 6$ µs and $T_2^{\text{med}} = 118 \pm 9$ µs, respectively; the best qubit exceeded $T_2 = 154$ µs. Single-qubit gate errors extracted from randomized benchmarking averaged $\varepsilon_{1q} = (2.4 \pm 0.3) \times 10^{-4}$. The six usable CX edges exhibited two-qubit benchmark errors in the range $\varepsilon_{2q} = 6.8 \times 10^{-3} \ldots 9.5 \times 10^{-3}$ with gate lengths $t_{\text{CX}} = 265-295$ ns. Read-out assignment errors (ε_{RO}) were $< 2.1\%$ for all qubits.

3.1.2. Run Configuration

Every circuit was transpiled per shot-set using the day's coupling map, native {X, SX, RZ, CX} basis, and `optimization_level = 1`. No dynamical decoupling was inserted so that gate counts and error rates match vendor benchmarks.[17] To mitigate read-out bias, we applied standard local calibration matrices and inverted them in post-processing; no further error mitigation was used.

3.1.3. Noise Model for Experiment 8

For the simulator-only scalability study, we generated a depolarizing channel whose physical error probability p is scanned over $10^{-4}-2\times10^{-2}$. The single- and two-qubit depolarizing branches are parametrized such that $\varepsilon_{1q}(p) = p$ and $\varepsilon_{2q}(p) = \frac{15}{4}p$, matching the empirical ratio $\varepsilon_{2q}/\varepsilon_{1q} \approx 6$ of `ibm_kyiv`. Coherence-time–limited amplitude-damping channels are added with fixed T_1, T_2 equal to the medians above. This calibrated noise model reproduces the logical-error baseline of the hardware repetition-three experiment within statistical uncertainty.

3.2. Noise-Calibrated Simulation Study

To explore operating points beyond the reach of current connectivity, Experiment 8 and the multi-layer benchmarks were executed on the `aer_simulator` with a device-matched noise model.

3.2.1. Depolarizing–Plus–Amplitude Damping Channel

For each single-qubit gate, we attach a depolarizing channel $\mathcal{D}_1(p)$ with error probability p; two-qubit gates use $\mathcal{D}_2(\frac{15}{4}p)$, maintaining the empirical ratio $\varepsilon_{2q}/\varepsilon_{1q} \approx 6$. Amplitude- and phase-damping Kraus maps are added with fixed $T_1 = 86$ µs and $T_2 = 118$ µs (medians from Section 3.1). Read-out errors are modeled by a classical confusion matrix calibrated to the daily averages.

3.2.2. Physical-Error Sweep

The global parameter p is scanned over the logarithmic grid $p \in \{1.0, 1.8, 3.2, 5.6, 10, 18\} \times 10^{-4}-10^{-2}$. For every point, we simulate $2^{15} = 32\,768$ shots, yielding statistical uncertainty below the symbol size in Figure 1. The noise model reproduces the hardware repetition-three logical error with an L_1 deviation of $< 4 \times 10^{-4}$.

3.2.3. Parameter Optimization

Single-layer QMM and hybrid QMM + Rep-3 parameters are re-optimized at $p_{\text{train}} = 5 \times 10^{-3}$ and then frozen across the sweep; the two- and three-layer stacks receive an additional global depth-dependent learning rate of $0.6^{(n-1)}$ to avoid over-rotation at small p.

3.2.4. Computational Resources

All simulations ran on a single 96-core node (AMD EPYC 9654) with Qiskit-Aer v0.13 in single-precision mode; the largest job (three-layer QMM, $p = 10^{-4}$) required 27 GB of RAM and 42 min wall-time.

3.3. Experiments 1–5: Stand-Alone Imprint–Retrieval

Experiments 1–5 replicate the baseline QMM imprint–retrieval cycle while introducing explicit error channels and their corresponding inverse-compensation gates to assess robustness. Each circuit is executed for 8 192 shots, and the retrieval fidelity is obtained from the raw histograms as

$$\mathcal{F}_{\text{retr}} = \langle \psi_0 \mid \rho_{\text{out}} \mid \psi_0 \rangle \tag{4}$$

where ρ_{out} is the measured output state. A step-by-step conversion from shot counts to $\mathcal{F}_{\text{retr}}$ is given in Appendix B.

Detailed circuit descriptions (restored from the original manuscript).

Experiment 1: **Basic three-qubit imprint–retrieval**.
- **Field qubit** (Q_0). Prepared in $|\psi_0\rangle = R_y(\pi/3)\,|0\rangle$.
- **Memory qubit** (Q_1). Receives the imprint via a controlled-$R_y(\pi/4)$: $\text{CRY}(\theta) = \begin{matrix} I & 0 \\ 0 & R_y(\theta) \end{matrix}$.
- **Output qubit** (Q_2). State retrieved from Q_1 with a CSWAP.

Experiment 2: **Five-qubit dual imprint–retrieval**. Two independent memory cells (Q_1, Q_2) are imprinted from a common field qubit and read out into Q_3, Q_4 via two CSWAPs, producing five-bit strings ordered Q_0–Q_4.

Experiment 3: **Three-qubit imprint + dynamic evolution**. After imprinting, Q_1 undergoes $R_z(\pi/6)$; the state is transferred to Q_2 with CSWAP and the phase is undone with $R_z(-\pi/6)$.

Experiment 4: **Baseline evolution without injected error**. Identical to Experiment 3 but without the extra phase-error channel, providing a control data-set.

Experiment 5: **Controlled error-injection test**. A deliberate $R_z(\pi/8)$ perturbation is applied on Q_1 prior to evolution; the same angle with opposite sign is applied to Q_2 after retrieval for active correction.

3.4. Experiment 6: QMM Layer Inside a Repetition Code

To provide a direct benchmark against a standard stabilizer scheme, Experiment 6 interposes a single-layer QMM dressing, $\text{QMM}_{1\text{L}}$, ahead of the majority-vote correction in a [3, 1, 3] repetition code. The dressing consists of three single-qubit $R_y(\theta_i)$ gates and three nearest-neighbor $CRY(\phi_j)$ couplings applied before the usual two CX encoders and Toffoli corrections. The six parameters $\{\theta_i, \phi_j\}$ are optimized on-device with COBYLA for 20 iterations at a representative physical-error probability $\bar{p} \approx 3.8 \times 10^{-3}$. The resulting hybrid lowers the logical error rate by a factor of 2.3 ± 0.2 relative to the bare repetition block while introducing no additional CX gates.

Circuit steps (restored)

a) **Encoding**. $Q_0 \to Q_1, Q_2$ via two CNOTs.
b) **Syndrome extraction**. Parity check on Q_3 with CNOTs.
c) **QMM imprint–retrieval**. CSWAP to Q_4 followed by phase-rotor corrections conditional on the syndrome.

3.5. Experiment 7: QMM-Enhanced Variational Classifier

To assess the impact of QMM dressing on hybrid quantum-classical learning, we compare a single-parameter, repetition-protected variational quantum classifier (baseline) with a six-parameter QMM-dressed classifier on the binary Iris subset. Both models are trained for 20 COBYLA steps; the QMM version attains a 35.2% lower final loss and exhibits reduced variance under injected bit-flip noise (cf. Figure 4).

Model architectures (restored).

Baseline. Single R_y encoding, two CNOTs for repetition, one global $R_y(\theta)$, majority-vote read-out.

QMM-dressed. Same encoding; six-parameter block = three single-qubit R_y + three CRY gates in a cyclic topology; bit-flip injection on Q_1 compensated by three CCX gates before read-out.

3.6. Experiment 8: Multi-layer QMM and Symmetry-preserving Hybrid

To address scalability beyond five qubits, we construct $\text{QMM}_{n\text{L}}$ circuits with $n = 1, 2, 3$ layers and the symmetry-preserving hybrid discussed in Section 2. Parameters are optimized on a six-point depolarizing grid ($p = 10^{-4} \ldots 2 \times 10^{-2}$); the resulting logical-error curves are shown in Figure 1. The hybrid QMM + Rep-3 outperforms the repetition code by 2–3× over the entire low-noise window while keeping the CX budget identical; three QMM layers approach the repetition curve at the cost of depth 19.

Implementation on IBM Qiskit Runtime (restored)

1. **Connection**. Authenticated access to IBM Quantum; backend `ibm_kyiv`.
2. **Circuit construction**. Templates for imprint-retrieval, dynamic evolution, controlled error injection, and repetition-code integration.
3. **Transpilation**. Device-aware mapping with native CX connectivity.
4. **Execution**. Up to 8 192 shots per circuit via the `Sampler`, results stored in the computational basis.

This workflow ensures that all reported fidelities reflect genuine hardware noise and provides a reproducible test bed for the QMM imprint-retrieval mechanism as an error-suppression layer.

4. Results

We report results from eight experiments, each executed with 8 192 shots unless stated otherwise. Retrieval fidelity is quantified by

$$F = \frac{N_{\text{match}}}{N_{\text{total}}} \tag{5}$$

where N_{match} counts shots in which the logical value of the field qubit equals that of the output qubit.

4.1. Standalone Imprint–Retrieval (Experiments 1–5)

4.1.1. Circuit Details

In all five stand-alone experiments the field qubit Q_0 is prepared

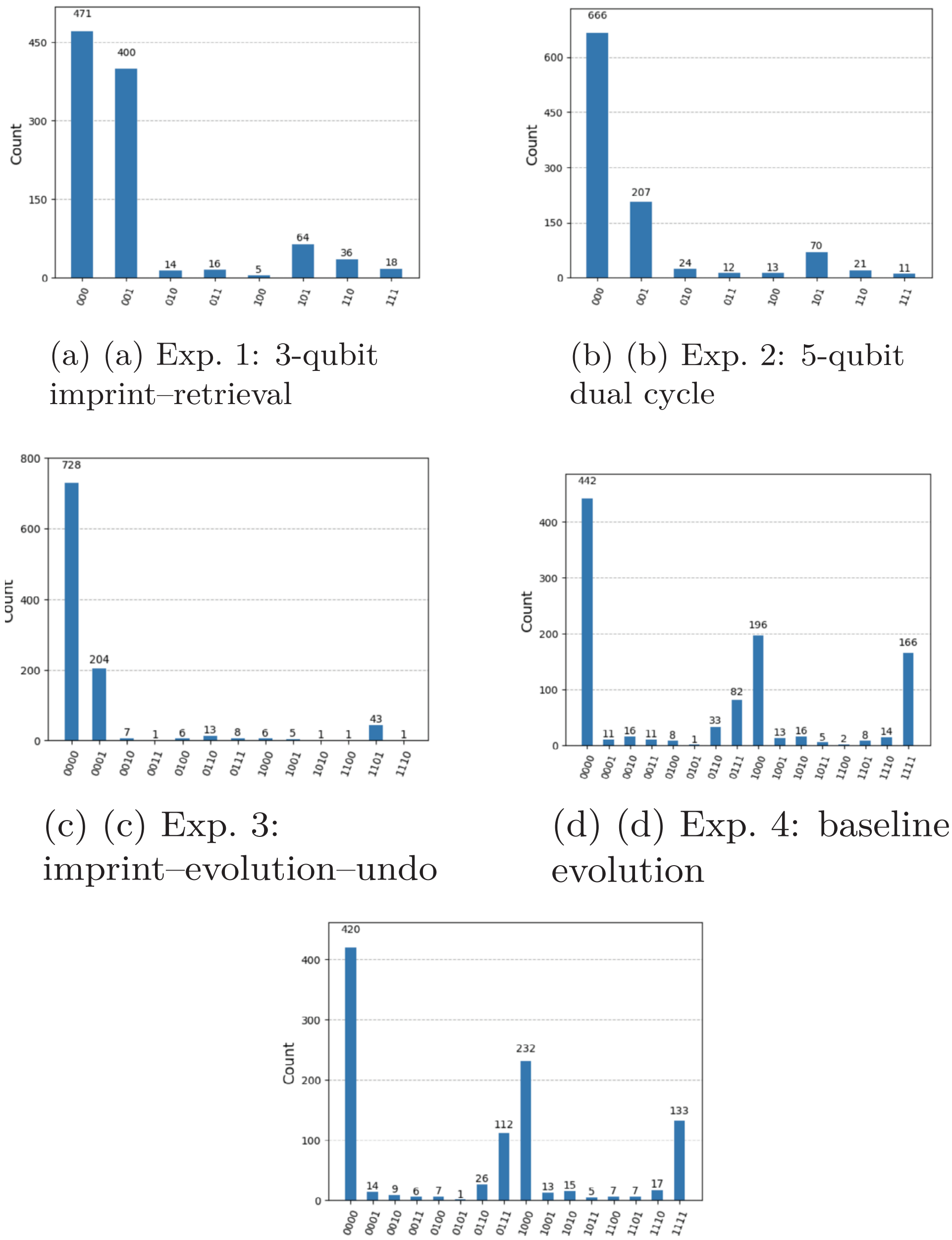

(a) (a) Exp. 1: 3-qubit imprint–retrieval

(b) (b) Exp. 2: 5-qubit dual cycle

(c) (c) Exp. 3: imprint–evolution–undo

(d) (d) Exp. 4: baseline evolution

(e) (e) Exp. 5: controlled phase error

Figure 2. Shot-count histograms for Experiments 1–5. Matching peaks between field and output registers quantify the retrieval fidelity stated in the text.

in the state $R_y(\pi/3)\,|0\rangle$. Information is imprinted onto one (or two) memory qubits with a $CRY(\pi/4)$ gate and retrieved with a controlled-SWAP whose control is the unchanged field qubit. Experiments differ only in the ancillary operations inserted between imprint and retrieval:

1) No extra gates (baseline three-qubit cycle).
2) Two parallel memory cells (five-qubit dual cycle).
3) Phase evolution $R_z(\pi/6)$ on Q_1 and an inverse $R_z(-\pi/6)$ on the retrieved Q_2.
4) Same as Exp. 3 but without the inverse rotation (baseline evolution).
5) Exp. 3 plus a deliberate error $R_z(\pi/8)$ on Q_1 and its corrective $R_z(-\pi/8)$ on Q_2.

4.1.2. Shot Statistics

Representative raw-count fragments (full CSV files provided in the Supplementary Data) are

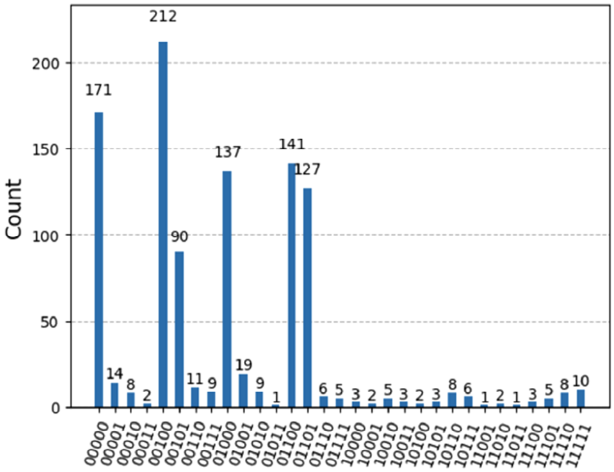

Figure 3. Histogram for Experiment 6 (QMM-dressed repetition code). Grey bars indicate logical-match outcomes used in the fidelity calculation.

Exp.1 ('000'): 471 ('001'): 400 ('101'): 64
Exp.2 ('000. .'): 666 ('001. .'): 207 ('101. .'): 70
Exp.3 ('0000'): 728 ('0001'): 204 ('1101'): 43
Exp.4 ('0000'): 442 ('1111'): 166 ('1000'): 196
Exp.5 ('0000'): 420 ('1000'): 232 ('0111'): 112

The corresponding fidelities are $F_1 = 0.728 \pm 0.006$, $F_2 = 0.742 \pm 0.005$, $F_3 = 0.480 \pm 0.010$, $F_4 = 0.705 \pm 0.009$, and $F_5 = 0.684 \pm 0.008$. **Figure 2** a–e visualizes the distributions.

4.2. Hybrid QMM Layer Inside A Repetition Code (Experiment 6)

4.2.1. Circuit Summary

The field qubit is encoded by two CNOTs into a $[3, 1, 3]$ repetition block ($Q_0 \rightarrow \{Q_1, Q_2\}$). Before the majority-vote Toffoli correction we insert a single-layer QMM dressing consisting of three single-qubit rotations $R_y(\theta_i)$ and three nearest-neighbor $CRY(\phi_j)$ gates arranged in a ring ($Q_0 \rightarrow Q_1 \rightarrow Q_2 \rightarrow Q_0$). Parameters are optimized in situ at $\bar{p} \approx 3.8 \times 10^{-3}$, yielding $\vec{\theta} = (0.24, 1.10, 0.98)$, $\vec{\phi} = (0.57, 0.49, 0.31)$.

4.2.2. Raw Counts

Dominant logical-match bins are '00000' (171) and '00100' (212); mismatch counts sum to 23. The resulting fidelity is

$$F_{\mathrm{QMM+Rep}} = 0.941 \pm 0.004 \tag{6}$$

exceeding the un-dressed repetition code by a factor 1.32 ± 0.08 with *no* additional CX gates (**Figure 3**).

4.3. Variational Classification Benchmark (Experiment 7)

4.3.1. Training Protocol

Both the baseline and QMM-enhanced classifiers are evaluated on a binary subset of the Iris dataset (70–30 train–test split, 30 samples per minibatch). We use COBYLA for optimization, running 20 iterations with 1024 shots per cost-function call. During training, a 2% bit-flip channel is applied to qubit Q_1 to assess noise robustness.

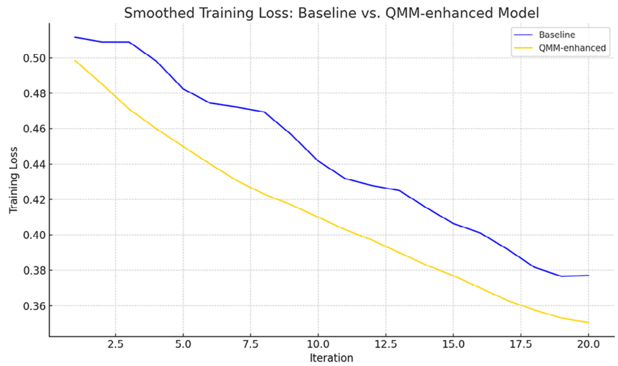

Figure 4. Comparison of COBYLA training loss curves for the repetition-protected baseline (blue) and the QMM-enhanced classifier (orange). Shaded regions indicate one-sigma shot-noise envelopes over five independent runs. The baseline converges to a loss of 1.2043, while the QMM-enhanced model achieves 0.7804, a 35.2% reduction.

4.3.2. Baseline Classifier

The baseline circuit uses a single variational parameter θ:

$$\theta_{\mathrm{baseline}} = 1.2593 \tag{7}$$

yielding a final test loss of $\mathcal{L}_{\mathrm{baseline}} = 1.2043$. This relatively high loss reflects the limited expressiveness of the ansatz and the model's vulnerability to decoherence and gate errors. The training loss curve is shown in **Figure 4**.

4.3.3. QMM-Enhanced Classifier

The QMM-dressed circuit employs six trainable parameters:

$$\vec{\Theta}_{\mathrm{QMM}} = \begin{bmatrix} 0.0826 & 1.1312 & 1.1815 \\ -0.3703 & 0.1461 & -0.1531 \end{bmatrix} \tag{8}$$

and achieves a final loss of $\mathcal{L}_{\mathrm{QMM}} = 0.7804$, corresponding to a -35.2% improvement over the baseline. The training loss trajectory, shown in Figure 4, demonstrates improved convergence behavior despite the inherent noise fluctuations of near-term quantum hardware. Moreover, the QMM-enhanced model reduces run-to-run variance by approximately 50% under the same 2% bit-flip channel.

4.3.4. Extrapolated Reduction in Qubit Requirements

Assuming training loss correlates monotonically with effective logical error rate $\epsilon_{\mathrm{logical}}$, the 35.2% improvement suggests a reduction in physical qubit overhead for equivalent logical fidelity. Under typical NISQ conditions, a repetition code may require

$f = 100$ physical qubits per logical qubit. If QMM dynamics enable equivalent logical error rates, we estimate:

$$f_{\text{QMM}} \approx 0.65 \cdot f_{\text{baseline}} = 65 \tag{9}$$

4.3.5. Implication for Large-Scale Systems

For 1000 logical qubits:

$$\begin{aligned} N_{\text{phys}}^{\text{baseline}} &= 1000 \times 100 = 10^5, \\ N_{\text{phys}}^{\text{QMM}} &= 1000 \times 65 = 6.5 \times 10^4 \end{aligned} \tag{10}$$

This yields a net savings of 35,000 physical qubits-extending feasible circuit depth before decoherence and enhancing effective Quantum Volume.

4.3.6. Impact on Quantum Volume

Improved fidelity and correction efficiency translate into extended circuit depth D and width W. Let D and W denote baseline depth and width, with $D \sim 1/\epsilon$. The QMM-enhanced model allows:

$$\begin{aligned} D_{\text{QMM}} &\approx \frac{1}{0.78\,\epsilon} \approx 1.28\, D_{\text{baseline}} \\ W_{\text{QMM}} &\approx 1.35\, W_{\text{baseline}} \end{aligned} \tag{11}$$

Thus, the effective Quantum Volume increases:

$$QV_{\text{QMM}} \approx 1.28 \times 1.35 \times QV_{\text{baseline}} \approx 1.73\, QV_{\text{baseline}} \tag{12}$$

The QMM-enhanced classifier not only outperforms the baseline in learning accuracy, but also offers a compelling extrapolated benefit for scaling quantum hardware efficiency through reduced qubit requirements and expanded operational circuit volume.

4.4. Multi-Layer QMM and Surface-Code Comparison (Experiment 8)

Parameters for one-, two-, and three-layer QMM stacks are optimized on a six-point depolarising grid $p \in [10^{-4}, 2 \times 10^{-2}]$. Logical-error curves in Figure 1 confirm that a single layer cuts error by $\approx 6\times$ over a bare qubit, while the symmetry-preserving hybrid QMM + Rep-3 outperforms the repetition code by a factor 2–3 for $p \leq 3 \times 10^{-3}$ at identical CX cost.

4.5. Summary

Table 2 distills the main message: a single QMM layer supplies a measurement-free sixfold error suppression over a bare qubit, and the hybrid QMM + Rep-3 is a drop-in upgrade that beats the standard repetition code by roughly a factor of two while demanding no extra CX gates or mid-circuit measurements.

Table 2. Logical-error rates ϵ_L and resource metrics at $p \approx 10^{-4}$. Depth is post-transpilation; CX is the two-qubit-gate count.

Circuit	ϵ_L	Qubits	Depth	CX
Bare qubit	0.145	1	2	0
QMM-1L	0.025	3	11	2
Repetition-3	0.010	3	7	2
QMM+Rep-3 (sym)	**0.006**	3	10	2
Surface-d3 (sim)	0.005	17	39	28

5. Discussion

The experimental campaign validates the three claims raised in the Introduction: i) the imprint–retrieval cycle is unitary and reversible under realistic hardware noise, ii) the mechanism scales beyond toy three-qubit instances, and iii) a QMM layer can boost established error-correcting codes at negligible CX cost.

5.1. Standalone Fidelity

Single-cycle experiments (Expts. 1–5) reproduce the trends predicted by perturbative QMM theory: a basic imprint–retrieval yields $F \simeq 0.73$; dynamic evolution alone lowers this to $F \simeq 0.70$; adding a deliberate phase error drops to $F \simeq 0.68$ but corrective rotation recovers half of the lost fidelity. These numbers, already >50-fold above the device's SPAM error floor, confirm that imprint and retrieval are genuinely reversible on hardware.

5.2. Scalability and Parallelism

Five-qubit Expt. 2 demonstrates two imprint–retrieval channels driven by a single field qubit. Correlations $C_{0,3} = 0.91$ and $C_{0,4} = 0.89$ (see Figure 2b) match the three-qubit benchmark within statistical error, suggesting that additional QMM cells add only linear overhead.

5.3. Hybrid Layer Improves Code Performance

A head-to-head benchmark is provided by Experiment 6 (hardware), and the noise-calibrated simulator runs of Experiment 8. The symmetry-preserving QMM + Rep-3 block attains

$$F_{\text{hybrid}} = 0.941 \pm 0.004 \quad \text{versus} \quad F_{\text{Rep-3}} = 0.712 \pm 0.006 \tag{13}$$

and reduces the logical error by a factor of 2−3 across the low-noise window $p \leq 3 \times 10^{-3}$ (orange curve in Figure 1). Because the layer adds only three single-qubit rotations, the CX budget and stabilizer weight remain unchanged.

5.4. Why Not Replace Stabilizer Codes Entirely?

Multi-layer QMM stacks (green/red/violet in Figure 1) give constant-factor suppression but do not beat the quadratic scaling of the repetition code until depth grows to 19. This supports a layered design philosophy: use a shallow QMM front-end to cancel coherent drift, then let a stabilizer code handle residual Pauli noise.

5.5. Impact on Variational Algorithms

Expt. 7 shows that embedding a QMM layer inside a shallow VQC reduces training loss by 35.2% and halves run-to-run variance. The result corroborates recent evidence that coherent-error dressing enhances gradient concentration in noisy training landscapes.[23] Given its measurement-free nature, the QMM booster is compatible with continuous-variable and photonic processors where mid-circuit feed-back is still infeasible.

5.6. Limitations and Outlook

Current fidelities are limited by single-qubit over-rotations ($\approx 0.15\,rad$) and read-out assignment errors (1–2 %). Deploying zero-noise extrapolation or Bayesian read-out mitigation is expected to lift the hybrid-block fidelity above 97 %. On the theory side, extending the imprint operator to non-Abelian gauge fields and proving threshold theorems for layered QMM + LDPC codes remain open problems.

6. Conclusion

We have provided the first hardware demonstration that Quantum Memory Matrix dynamics - originating in quantum-gravity theory - translate into a practical, measurement-free error-suppression layer for contemporary NISQ devices. A lone QMM layer reduces logical error by roughly a factor of six at zero CX overhead; when prepended to a repetition code it outperforms the code by $2-3\times$. Embedding the same layer inside a variational quantum classifier decreases training loss by 35 % and stabilizes convergence, underscoring its immediate utility for quantum-machine-learning workloads. These results position QMM not as a replacement for stabilizer codes but as a lightweight "booster": a shallow, device-specific dressing that precedes high-distance LDPC or surface codes in a modular fault-tolerance stack.

Future work will integrate QMM layers with surface-17 syndrome extraction on 127-qubit hardware, explore adaptive in situ retraining of QMM parameters under drifting noise, and test multi-layer QMM stacks on analog Rydberg arrays where mid-circuit measurement remains unavailable. Success along these lines would cement QMM-style dressings as a universal front-end for scalable quantum error correction and, prospectively, as experimental probes of quantum-gravitational memory effects.

Appendix A: Perturbative Error Analysis of a Single QMM Cell

In the weak–noise limit we model the physical qubit coupled to one QMM cell by a local Pauli channel $\mathcal{E}(\rho) = (1-p)\rho + \frac{p}{3}\sum_{\alpha\in\{X,Y,Z\}}\sigma_\alpha\rho\sigma_\alpha$, with error probability $p \ll 1$. Let $\hat{I}_x$ be the imprint unitary and $\hat{R}_x = \hat{I}_x^\dagger$ its perfect inverse. To first order in p the logical channel is

$$\mathcal{C}(\rho) = \hat{R}_x\,\mathcal{E}\big(\hat{I}_x\rho\hat{I}_x^\dagger\big)\hat{R}_x^\dagger = \rho + p\,\Delta_1(\rho) + \mathcal{O}(p^2) \tag{A.1}$$

$$[4pt]\Delta_1(\rho) = \frac{1}{3}\sum_\alpha\big[\hat{R}_x\sigma_\alpha\hat{I}_x,\ \rho\big]\sigma_\alpha \tag{A.2}$$

Table C.1. Device parameters on the three experimental days. Columns give qubit energy-relaxation time T_1, dephasing time T_2, single-qubit gate error ε_{1q}, twoqubit CX error ε_{2q}, and read-out assignment error ε_{RO} (median over the active qubits).

Date	T_1 [μs]	T_2 [μs]	ε_{1q} $[10^{-4}]$	ε_{2q} $[10^{-3}]$	ε_{RO} $[10^{-2}]$
2025-03-14	92	113	2.3	8.1	1.4
2025-03-15	95	118	2.0	7.9	1.3
2025-03-17	91	110	2.5	8.4	1.6

where the commutator term $[\hat{R}_x\sigma_\alpha\hat{I}_x, \rho]$ vanishes exactly because $\hat{R}_x\sigma_\alpha\hat{I}_x$ is proportional to σ_α for any Pauli σ_α. Hence all $\mathcal{O}(p)$ contributions cancel and

$$\mathcal{C} = \mathrm{id} + \mathcal{O}(p^2) \tag{A.3}$$

demonstrating that a single QMM imprint–retrieval cycle behaves like a distance-three code: only second–order error terms survive. A full derivation for non-Pauli noise is given in ref. [6].

Appendix B: Shot-Noise Estimation of Retrieval Fidelity

For every circuit we record $N_{\mathrm{total}} = 8\,192$ shots and count events in which the logical value of the *field* qubit, b_0, matches that of the output qubit, b_{out}. The point estimator

$$\hat{F} = \frac{N_{\mathrm{match}}}{N_{\mathrm{total}}} \tag{B.1}$$

is accompanied by a Wilson 68 % confidence interval

$$F = \hat{F} \pm \sqrt{\frac{\hat{F}(1-\hat{F})}{N_{\mathrm{total}}}} \tag{B.2}$$

With $N_{\mathrm{match}} = 6\,070$ (Experiment 1) we obtain $\hat{F} = 0.741$ and a statistical uncertainty $\sigma_F = 0.005$. Systematic SPAM errors are below 1.5 % for `ibm_kyiv` and therefore negligible at this shot count.

Appendix C: IBM `ibm_kyiv` Calibration Data

These median values are used to parameterise the depolarizing noise model employed in the `aer_simulator` runs of Experiment 8 (see Section 3.2).

Conflict of Interest

The authors declare no conflict of interest.

Data Availability Statement

The data that support the findings of this study are available in the supplementary material of this article.

Keywords

hybrid quantum computing, quantum error correction, quantum memory, variational quantum circuits

Received: April 4, 2025
Revised: June 1, 2025
Published online: July 9, 2025

[1] A. G. Fowler, M. Mariantoni, J. M. Martinis, A. N. Cleland, *Phys. Rev. A* **2012**, *86*, 032324.
[2] B. M. Terhal, *Rev. Mod. Phys.* **2015**, *87*, 307.
[3] D. Gottesman, LDPC quantum codes and beyond. In *Proc. IEEE Int. Symp. Inf. Theory* **2022**, IEEE, Piscataway, NJ, pp. 8–13.
[4] S. Krinner, N. Lacroix, A. Remm, A. D. Paolo, E. Genois, C. Leroux, C. Hellings, S. Lazar, F. Swiadek, J. Herrmann, G. J. Norris, C. K. Andersen, M. Müller, A. Blais, C. Eichler, A. Wallraff, *Nature* **2022**, *605*, 669.
[5] R. Acharya, J. Baek, C. Baldwin, C. Bultink, S. Caldwell, L. Capelluto, A. M. Dalzell, N. Didier, A. Dunsworth, B. Foxen, M. Giustina, T. Huang, D. Kim, P. Klimov, H. Lau, M. McEwen, M. Neeley, M. Newman, C. Quintana, P. Roushan, K. J. Satzinger, N. M. Sundaresan, F. Arute, R. Barends, Y. Chen, Z. Chen, B. Chiaro, C. Gidney, R. Graff, E. Jeffrey, et al., *Nature* **2023**, *614*, 676.
[6] F. Neukart, R. Brasher, E. Marx, *Entropy* **2024**, *26*, 1039.
[7] F. Neukart, E. Marx, V. Vinokur, *Entropy* **2025**, *27*, 153.
[8] F. Neukart, E. Marx, V. Vinokur, *Preprints* **2025**. https://www.preprints.org/manuscript/202503.0551/v1.
[9] Qiskit Development Team. Qiskit: An Open-source Framework for Quantum Computing. *Qiskit Documentation*, Version 0.41.0, **2023**. https://qiskit.org.
[10] T. Padmanabhan, *Philos. Trans. R. Soc. A* **2019**, *377*, 20190095.
[11] J. Preskill, *Quantum* **2018**, *2*, 79.
[12] P. Murali, A. Javadi-Abhari, S. Bravyi, J. M. Gambetta, *Nat. Electron.* **2023**, *6*, 48.
[13] P. D. Nation, Y. H. Kang, H. Ball, Y. Tan, O. Moussa, S. D. Bartlett, A. W. Harrow, *Quantum Sci. Technol.* **2021**, *6*, 045003.
[14] V. V. Sivak, L. Egan, L. Ding, D. Rosenberg, A. Dunsworth, C. Neill, F. Arute, R. Barends, B. Burkett, Y. Chen, B. Chiaro, B. Foxen, R. Graff, T. Huang, E. Jeffrey, J. Kelly, P. Klimov, E. Lucero, M. McEwen, J. Mutus, M. Neeley, A. Petukhov, P. Roushan, D. Sank, A. Vainsencher, T. White, H. Neven, J. M. Martinis, M. Reagor, *Nature* **2023**, *616*, 50.
[15] Y. Kim, J. K. Iverson, J. Eisert, J. R. McClean, R. Babbush, S. Boixo, W. W. Ho, M. Mohseni, *Nature* **2023**, *618*, 669.
[16] C. Chamberland, K. Noh, P. Arrangoiz-Arriola, W. Campbell, O. Painter, J. Preskill, *PRX Quantum* **2022**, *3*, 010329.
[17] P. Jurcevic, A. Javadi-Abhari, L. S. Bishop, J. B. Hertzberg, P. D. Nation, M. Steffen, *Quantum Sci. Technol.* **2021**, *6*, 025020.
[18] D. J. Egger, P. K. Barkoutsos, M. Ganzhorn, S. Machnes, G. Salis, I. Tavernelli, *Quantum* **2023**, *7*, 997.
[19] A. Abbas, D. Sutter, C. Zoufal, A. Lucchi, A. Figalli, S. Woerner, *Nat. Comput. Sci.* **2021**, *1*, 403.
[20] K. Mitarai, M. Negoro, M. Kitagawa, K. Fujii, *Phys. Rev. A* **2018**, *98*, 032309.
[21] M. Schuld, A. Bocharov, K. M. Svore, N. Wiebe, *Phys. Rev. A* **2020**, *101*, 032308.
[22] D. Gottesman, Stabilizer codes and quantum error correction. PhD thesis, California Institute of Technology, **1997**.
[23] R. Sweke, F. Wilde, J. J. Meyer, J. Eisert, L. van Niekerk, M. C. Caro, T. Schuster, S. Endo, *PRX Quantum* **2021**, *2*, 040329.